Controlling Thin Film Morphology Formation during Gas Quenching of Slot-Die Coated Perovskite Solar Modules

Kristina Geistert[1,2], Simon Ternes[1,2], David B. Ritzer[2], Ulrich W. Paetzold[1,2]*

[1] Light Technology Institute, Karlsruhe Institute of Technology (KIT), 76131 Karlsruhe, Germany

[2] Institute of Microstructure Technology, KIT, 76344 Eggenstein-Leopoldshafen, Germany

Abstract

Transferring record power conversion efficiency (PCE) >25 % of spin-coated perovskite solar cells (PSCs) from the laboratory scale to large-area photovoltaic modules requires significant advance in scalable fabrication techniques.[1–3] In this work, we demonstrate the fundamental interrelation between drying dynamics of slot-die coated precursor solution thin films and the quality of slot-die coated gas quenched polycrystalline perovskite thin films. Well defined drying

conditions are established using a temperature-stabilized, movable table and a flow-controlled, oblique impinging slot nozzle purged with nitrogen. The accurately deposited solution thin film on the substrate is recorded by a tilted CCD camera, allowing for in situ monitoring of the perovskite thin film formation. With the tracking of crystallization dynamics during the drying process, we identify critical process parameters needed for the design of optimal drying and gas quenching systems. In addition, defining different drying regimes, we derive practical slot jet adjustments preventing gas backflow and demonstrate large-area, homogeneous and pinhole-free slot-die coated perovskite thin films that result in solar cells with PCEs of up to 18.6%. Our study reveals key interrelations of process parameters, e.g. the gas flow and drying velocity, and the exact crystallization position with the morphology formation of fabricated thin films, resulting in a homogeneous performance of corresponding solar $50\times50\,\text{mm}^2$ mini-modules (17.2%) with only minimal upscaling loss. In addition, we validate a previously developed model on the drying dynamics of perovskite thin films on small-area for slot-die coated areas of $\geq100\,\text{cm}^2$. The study provides methodical guidelines for the design of future slot-die coating setups and establishes a step forward to a successful transfer of industrial-scale deposition systems beyond brute force optimization.

1. Introduction

Nowadays, the necessity of an immense push to fight climate change and reduce the carbon footprint of the global economy is recognized by the vast majority of policy makers. Consequently, the demand for solar power plants as well as domestic photovoltaic (PV) panels is expected to increase rapidly in the following years. Next generation PVs encompassing new semiconductor materials experience a great interest in research and industry.[4–6] Besides cadmium telluride

(CdTe), organic PV, copper indium gallium selenide (CIGS) and gallium arsenide (GaAs), which are already partially commercialized, perovskite solar cells (PSCs) are one of the most promising emerging thin film technologies.[7] The reason for the popularity of hybrid organic–inorganic perovskite semiconductor materials is their outstanding optoelectronic performance, including high absorption coefficients enabling thin film fabrication, long charge carrier diffusion lengths, high defect tolerance as well as their bandgap tunability and the ease and potential of fabrication by solution-based deposition techniques[8]. These properties enabled the development of PSCs with high power conversion efficiencies (PCEs) up to 26.1 %.[9,10]

To date, the vast majority of PSCs reported in literature exhibit laboratory-scale device area ($\sim$0.1-1 cm^2) and are commonly processed by non-scalable deposition techniques, which is mostly spin coating. Thus, one major challenge of the technology is upscaling the deposition of homogeneous high-quality thin films to large areas (≥ 100 cm^2) without performance loss using industry-relevant deposition techniques.[2,11–14] On this account, the present work deals with the solution processing of hybrid perovskite thin films by the scalable technique of slot-die coating (SDC). SDC promises scalable, material, and cost-efficient deposition of perovskite thin films on a wide range of substrate types.[15,16] Recent publications successfully integrate the industrial adaptable process of SDC for two-terminal wide bandgap halide perovskite/c-Si tandem solar cells.[11,17] To date, slot-die coated methylammonium-free perovskite modules reach a PCE of up to 16.2 % (active area of 57.5 cm^2), while the current record in PCE of a solution-processed module, 17.9 %, is held by Panasonic who inkjet-printed the perovskite absorber thin films.[18,19] These values still lag behind the record of spin-coated laboratory-scale PSCs of 25.8 %. When scaling PV, loss of active area due to module scribing and interconnection resistances cannot be avoided.[7,14] However, compared to concurrent thin film modules involving similar architectures,

the upscaling losses in perovskite PV modules remain high.[1] The reason is that industrial deposition techniques, such as SDC, are yet complex to control during the entirety of the perovskite thin film formation due to diverse challenges on the microscopic scale such as crystallization dynamics and on the macroscopic scale such as wet thin film fluid dynamics. While the morphology formation and thickness of perovskite thin films during the spin-coating process is reliably regularized by the continuous centrifugal force arising from spinning, the complex fluidic, drying and crystallization dynamics of perovskite solution thin films in scalable deposition and quenching techniques are not yet fully understood.[20,21] Because of thicker and less homogeneous solution thin films deposited via slot-die coating, compared to spin coated solution thin films, there is a high solvent content and increased drying time in these wet thin films. Consequently, the impact of drying related transport mechanisms and phenomena, such as the coffee ring effect is magnified in these thicker thin films.[22] Therefore, one of the most challenging parts of upscaling PSCs is the deposition of a perovskite thin film with a homogeneous morphology over a large area. The desired properties of such a thin film include full surface coverage without pinholes, low roughness, high crystallinity and low density of grain boundaries on the microscale, and the absence of coating defects or coffee-rings on large scales.[20,23]

An additional challenge of solution processed scalable techniques is selecting a proper quenching technique. The controlled and obligatory promptly induced nucleation of the perovskite thin film in the drying wet thin film is crucial to achieve high PCEs for solution processed multi-cation perovskite thin films.[12,24] In the context of solution processing of perovskite thin films, several methods are applied to induce a prompt nucleation, e.g., vacuum, antisolvent and gas quenching were demonstrated.[24] Thermal processes are usually not suitable for quenching, since they can not provide a fast, prompt nucleation and sufficient mass transfer of the solvents.[24] This

present study focusses on the gas-assisted quenching that is a promising scalable fabrication method to process high-efficiency cells without costly and complex handling of antisolvents.[25,26] Simultaneously, it is transferable to roll-to-roll (R2R) fabrication unlike vacuum induced quenching.[16,24] Altogether, gas quenching is a facile, reproducible, low-cost and easily transferable technique, thereby showing great potential in the application of highly-efficient large-area PSCs.[11,13,24,27]

For the induced crystallization during quenching, there is a specifically high mass transfer needed at the position where the wet thin film passes the critical solute concentration.[12] Gas quenching is an established drying technique that offers sufficiently high solvent mass transfer from the wet thin film to promptly remove the solvent and induce a rapid nucleation.[26–29] However, due to the complexity of the formation of polycrystalline perovskite thin films from the precursor solution, efficient strategies for process transfer require advancing the understanding of the involved dynamic processes. The goal is to identify appropriate quenching parameters which obtain the intended prompt crystallization but still do not disturb the high-quality homogeneity over large scales, e.g. via a strong gas flow. Controlling the formation of slot-die coated perovskite thin films is still a subject of current research due to complex drying and crystallization dynamics as well as entangled stages of drying, nucleation and grain growth.[30]

In response to the complexity of controlling the above mentioned perovskite coating and quenching on large areas, in situ monitoring of the perovskite process has been proposed.[12,15,28] Both, optical and x-ray based spectroscopic methods are common.[13,20,27,31] This work focusses on optical imaging as a cost-effective and fast way of surveilling the onset of the crystallization process on the lateral substrate area during the drying process of slot-die coated triple-cation

(methylammonium, formamidinium, and cesium) perovskite thin films. Simultaneously, we control the N_2-flow, such that it becomes possible to investigate the dependence on the monitored crystallization front on the nitrogen (N_2-) flow. Therefore, monitoring the quality of slot-die coated and gas quenched perovskite thin films reveal the correlation of the morphology formation as a function of the N_2-flow gas velocity. Specifically, part of the work deals with the methodology of monitoring and investigating gas-assisted conversion for the scalable deposition of suitable solvent systems to fabricate stable multi-cation perovskite thin films. Thereby, we validate the requirement of a moving high-pressure gas system as shown in a model of drying dynamics that was introduced by Ternes et al.[12] The model describes the thickness decrease of a perovskite thin film driven under a high-pressure slot jet of drying gas with constant velocity. The proposed model analyzes the impact of gas speeds and driving velocity from a fundamental view point, relying on accurate, quantitative prediction of the locally dependent heat transfer coefficients calibrated to thermochromic liquid crystals heat transfer measurements.[12,32]

In this context, this work introduces the in situ monitoring of gas-quenching is as a promising approach to substantiated fine-tuning of process parameters.[12,13,15,20,27] The evaluation of the morphology formation leads to crucial and concrete rectification work on the drying procedure. Additionally, this work validates the proposed model of drying dynamics based on local heat transfer measurements.[12] While the drying model is established and confirmed on small-area,[32] a demonstration and validation of this knowledge within *large-area* fabrication is to date still missing and will be of great relevance for the community of perovskite PVs. By validating the model on scalable substrates, predicting drying windows in terms of gas flow velocity and web speed, this study results in the successful fabrication of upscaled slot-die coated gas quenched solar cells and modules on large scales with only minimal upscaling losses. Confirming the correlation

of the quenching positions – which are indicated by recording a "drying front" with a CCD camera – and the morphology formation of the fabricated thin films as well as the performance of fabricated solar cells, this is a corner stone preventing expensive brute force optimization.
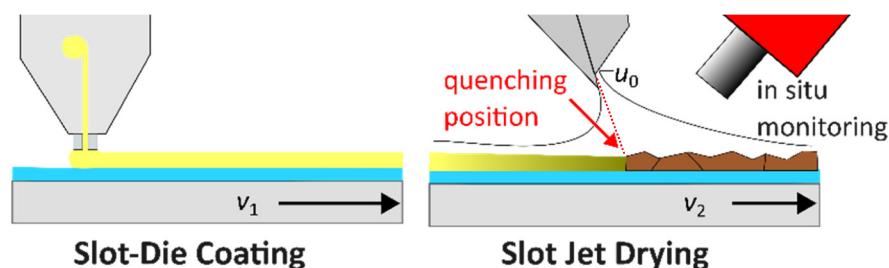
Figure 1. Schematic of slot-die coating (left) and subsequent dynamic gas-quenching (right), showing the broad deposition and dying method using two different velocities v_1 and v_2. The gas quenching is performed with a thin oblique impinging slot jet at height H_D, with a slot width of 50 µm ejecting N_2 with gas flow rate u_0. The dashed red line represents the maximum of gas projection, altering with the angle of the slot jet. The quenching position indicates where the critical solute concentration is exceeded and crystallization starts. The formation of the perovskite during gas quenching is monitored in situ with a scientific CCD camera. Further details are shown in Figure S1.

2. Results and Discussion

2.1. In situ monitoring of the "drying front"

In order to investigate the perovskite morphology evolution ($Cs_{0.1}(FA_{0.83}MA_{0.17})_{0.9}(I_{0.83}Br_{0.17})_3$ in DMF:DMSO 4:1) on large areas (i.e. $\geq 100\,cm^2$), we present a unique setup. In detail, we use the setup to correlate process parameter combinations (e.g. gas speed and drying velocity) as well as

the emerging quenching positions, where the critical solute concentration is exceeded (Figure 1), with the associated perovskite thin film quality. In first step, the perovskite solution is deposited by a 10 cm wide, fixed slot-die coater with a slot-die width (b_{SD} = 0.1 mm), slot-die gap (H_{SD} = 150 µm) and coverage-thickness optimized dispense rate (d_r = 1.55 ml min^{-1}) over the substrate on a movable table with temperature (T = 40 °C) with coating velocity v_1 (Figure 1, left). In a second step, the solution is dried with a fixed slot jet with a nozzle width of 10 cm, height H_D, angle β, slot width (b_D = 50 µm), gas flow rate u_0 and drying velocity v_2. The morphology formation of perovskite thin films is monitored and investigated in situ with a CCD camera during the gas quenching process (Figure 1, right). The camera is situated 20 cm behind the slot nozzle and mounted at a height of 15 cm and an angle of ~50° with focus on the area underneath the slot nozzle. With the camera, a video is recorded during the time the substrate is moved underneath the fixed slot nozzle, so that images of the visible drying process can be continuously extracted (see video S1 in Supporting Information). During the drying process, we define the line of quenching positions as "drying front" with a CCD camera, referring to the horizontal visual positions where enough solvent is vaporized such that the critical solute concentration is exceeded (see red indication of the quenching position (2D) on the right side in Figure 1). The "center line" is defined as the area directly underneath the maximum of gas projection (in Figure 1 congruous to the quenching position). In the following we will analyze the significance of the distance of the drying front from the center line.

For studying the morphology formation in the setup in Figure 1, we investigate the coating of a typical substrate (98x128 mm^2) at a coating velocity of 6 mm s^{-1}, a drying velocity of 2 mm s^{-1}, a nozzle height of 0.9 cm, an angle of ~15° and gas flow rate of 40 m s^{-1}. A photograph of the coated substrate is visible in Figure 2 (left). First, ribbing effects occur, which is a common

observation for large-scale slot-die coating. These small periodic height variations perpendicular to the coating direction in the wet-film thickness are observed when there is an unbalance in viscous and capillary forces between the precursor solution, slot-die head and substrate and may persist after solidifying.[21] The effects can be minimized by letting the wet film equilibrate for a longer time after coating. This is, however, destructive in the case of drying halide perovskite precursor solutions, because solvents need to be rapidly removed to avoid negative effects on the thin-film morphology. Further study goes beyond the scope of this work. A thorough study in terms of reducing the ribbing effect in another solvent system by reducing the ink viscosity is demonstrated in a recent publication of Li et al.[33]

Second, even to the bare eye, a distinct transition of thin film morphologies is visible (see video S1 in Supporting Information). In the beginning, the thin film appears diffusely reflective, then transitions into a dark, specular reflecting area and finally a gray diffuse area is visible. Later, we demonstrate that these morphologies indeed correspond to different microscopic morphologies and therefore, use optical imaging to verify the criteria for optimized perovskite thin film formation on larger areas. In order to understand the cause for the formation of different morphologies, we evaluate the images recorded with the camera depicted in Figure 1. The results are depicted on the right side of Figure 2. Remarkably, we find significant differences of the position of the drying front (horizontal visual positions where enough solvent is vaporized such that the critical solute concentration is exceeded, indicated as red line in Figure 2) at the exact times when the corresponding morphology evolved. In the beginning of the coating (orange boxes in Figure 2), the crystallization has not yet started and the drying front is situated a significant distance after the center line (area directly underneath the maximum of gas projection, indicated as green dotted line) is reached. We denote this drying regime in the following as "post-drying". At a later time,

when the specular reflecting morphology evolves, the drying is situated right at the center line. We denote this drying regime in the following as "instant-drying." When the drying front is situated a significant distance before reaching the center line, we denote the drying regime as "pre-drying".

The above observations, that enable to distinguish different drying regimes, confirm a correlation proposed in an earlier study by Ternes et al., which states that the morphology evolution is optimal exactly when there is a specifically high mass transfer needed at the position where the wet thin film passes the critical solute concentration to induce rapid drying and a high nucleation rate.[12] Such a high mass transfer is achieved only directly underneath the slot jet center.[32,34] We distinguish the drying and crystallization characteristics of slot-die coated perovskite absorber thin films dried via gas-quenching based on prior studies of local heat transfer measurements.[12] The observations depicted in Figure 2 are consistent with former studies of the drying dynamics which elaborates that the timing for gas quenching a blade coated wet thin film of the ink on a small-area substrate ($< 3\,cm^2$) is crucial for the formation of optimal perovskite thin film morphologies.[12,32] This work shows for the first time by direct in situ observation, that the position of the drying front (horizontal visual positions where enough solvent is vaporized such that the critical solute concentration is exceeded) with respect to the center line (area directly underneath the maximum of gas projection) of the slot jet indeed elucidates the drying dynamics during the morphology formation (Figure 2), preventing brute force optimization. Remarkably, we succeed in demonstrating the accurate correlation of the position of the drying front with the evolving thin film morphology. This interrelation validates that a certain threshold of mass transfer coefficient must be present at critical thin film thickness, which is correlated with the critical concentration/supersaturation.

The combination of the different drying states explained above on one substrate is determining for perovskite upscaling. We account their occurrence to the following difficulties that occur in batch-to-batch processing. Either the wet thin film shows small fluctuations and cannot be dried homogeneously without the prior fully evolved and 2-dimensional aligned meniscus, or the drying condition is not guaranteed fast enough, since the gas quenching can only be started, when the substrate is already underneath the slot. The reason for the latter is the gas backflow – the inevitable gas flow which goes in the opposite direction to the slot-die (SD) coater (see Figure S1 in the Supporting Information). When mistiming the onset of the gas flow, the gas flow can easily get underneath the substrate and lift the substrate from the movable table, overcoming the applied vacuum.

Moreover, the gas backflow is the reason for the phenomenon of the dominant pre-drying visible on the images in Figure 2 (red boxes). In the case of pre-drying the drying front is situated before the center line. Therefore, the mass transfer becomes gradually smaller and insufficient. In addition, the ribbing effect is more prominent in the pre-drying region, since the wet film has less time for self-equilibration. The gas backflow is almost inevitable, due to, e.g., disturbing but unavoidable components in the nozzle, the inside contour having edges and certain radii of curvature inducing stalling and turbulences of the gas flow as well as the tendency of air flowing from high to low pressure regions.[35,36] In consequence, the gas backflow of the slot jet naturally has a stronger effect on the rear part than on the front part of the substrate's wet thin film and causes pre-drying, resulting in an early nucleation and suboptimal thin film formation. Monitoring of the drying front reveals that the drying front is ahead of the center line due to the gas backflow of the slot jet (Figure 2, red frame). As a result, we learn that the position of the drying front correlates strongly with the quality of the evolving upscaled perovskite morphology, verifying the

model of drying dynamics by Ternes et al., which states, that a prompt crystallization at a critical thin film thickness is necessary for an optimal morphology formation.[12]
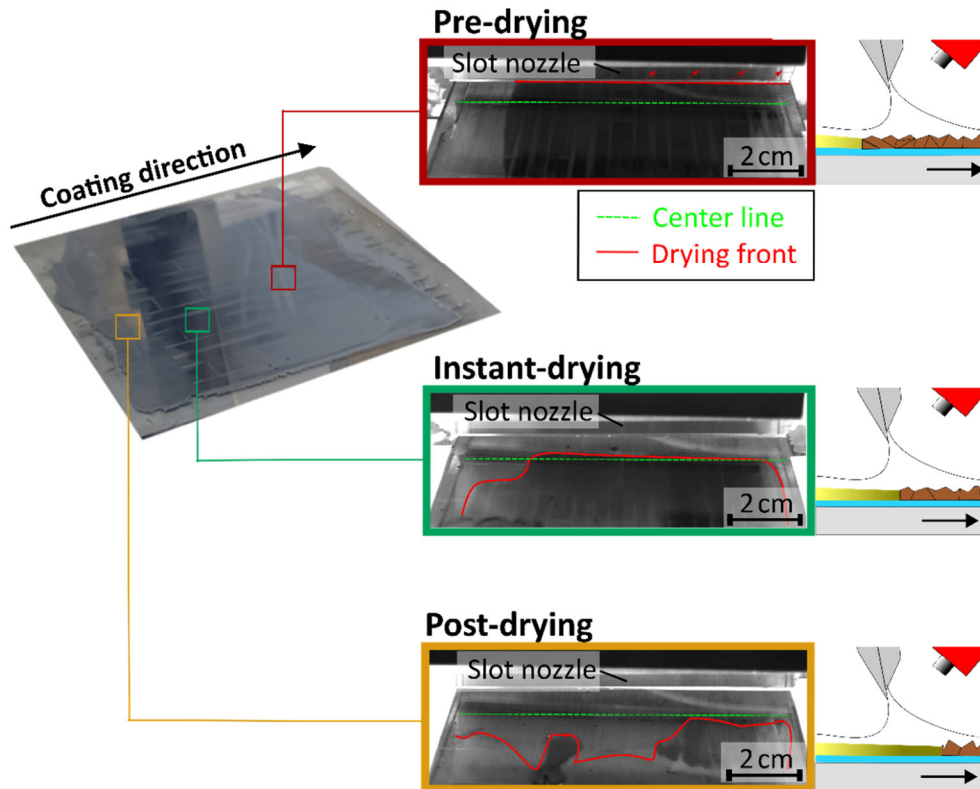
Figure 2. Photograph (images of recording camera/"frozen" in situ video, see video S1 in Supporting Information) of perovskite absorber thin film (>100 cm^2) fabricated with the setup shown in Figure 1 at the quenching gas flow velocity u_0 = 42 m s^{-1}, dynamic drying speed of 2 mm s^{-1} and nozzle height of 1.5 cm (left): The evolving morphology varies strongly in the beginning (orange square), center (green square) and end regions (red square). As shown in the example frames, this morphology variation can be explained by the different positions of the quenching ,i.e., crystallization onset. We define the visible line of crystallization onsets as "drying front" (red line). The "center line" (green dotted line) is defined as the area directly underneath the maximum of gas projection, close to the area directly underneath the slot nozzle.

In the beginning region of the substrate (bottom right, orange frame with an image of the recording camera at this time), the crystallization occurs behind the maximum gas projection (post-drying), in the center region (middle right, green frame with an image of the recording camera at this time), the crystallization occurs right at the center line (instant-drying), while in the end region of the substrate (top right, red frame with an image of the recording camera at this time), the crystallization occurs before the thin film reaches the center line, i.e., the maximum gas flow (pre-drying).

2.2. Correlation of drying behavior with surface morphology and device performance

As introduced in 2.1, large variations of the drying conditions are apparent on a single substrate processed with nominally accurate drying parameters. To determine the impact of the respective morphologies on the performance of perovskite solar cells, we fabricated test cells (due to clarity reasons, positions are only indicated in Figure 4) with all-scalable methods and an active area of $10.5\,mm^2$ based on the architecture ITO/2Pacz/Per/C60/BCP/Ag (see Experimental Section and Figure S5 Supporting Information). The devices are subsequently measured under a solar simulator (see Experimental Section). We further average the devices corresponding to the respective drying regimes introduced above.

As a result, we find that the variations of the drying front at different time-slots of the camera record (see Figure 2) correlate to significant differences in morphology and device performance (Figure 3). The mean PCE averaged over $102\,cm^2$ test devices increases by 4.6 % comparing the pre-drying (13.5 %) to the optimal regime of instant-drying (18.1 %) and latter increases 11.8 % comparing to the post-drying regime (6.3 %).

Consistent with the PCE trend and the analysis of perovskite morphology formation described in the last section, macroscopic investigations of the morphology via light microscopy (LM) reveal clearly that pinholes and inhomogeneities develop when the thin film is post-dried (Figure 3 a, orange framed LM image compared to green and red). Simultaneously, microscopic investigations reveal that grain sizes (diameter "d" in Figure 3 b) are reduced by a factor of 3 during pre-drying compared to the optimal instant-drying. Uncontrolled drying due to post-drying also leads to an overall reduced grain size in average additional to the more detrimental pinholes. Accordingly, champion JV-curves of cells (see Experimental Section) fabricated on respective areas of the substrate as well as the average PCEs confirm that the PCE has an optimum when the center line and drying front are at the same position (green) as well as that post-drying (orange) and the dominant pre-drying (red), result in a reduced cell efficiency (see Figure 3 c) and Table 1). Overall, the champion PCE of a cell fabricated with the optimized area reaches a high optimum value of 18.6 % compared to the reduced PCE of the pre-dried (14.5 %) and post-dried sample (8.6 %).

Post-drying is well known in literature to be inoperative for a controlled drying behavior.[27] The wet thin film dries in an uncontrolled manner without the facile and reproducible gas quenching technique. This insight is consistent with Figure 2, which specifically has the consequence that the drying front must not be delayed. Contrarily, the vital role in obtaining high-quality perovskite thin films becomes apparent in both cases of instant- and pre-drying (see corresponding LM images with green and red frames).

However, due to pre-drying, the nucleation starts too early, decreasing the overall grain size (seen in scanning electron microscope (SEM) surface images in Figure 3 b as "d"). As a result, the diffusion length of charge carriers is decreased. Therefore, the drying front must also not occur before the center line.
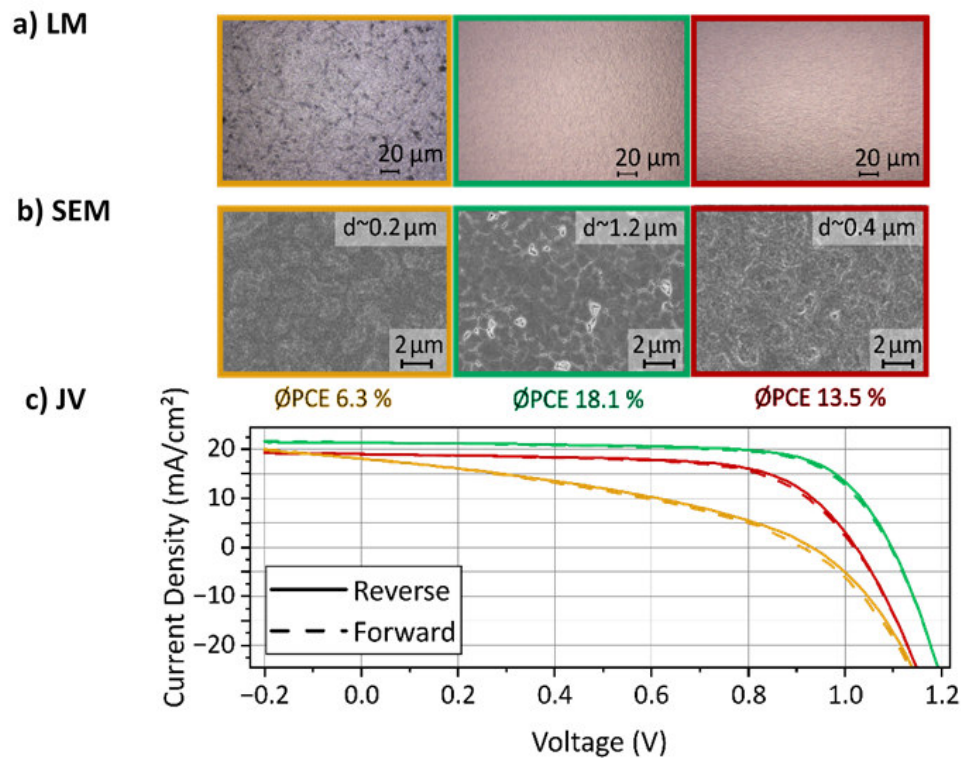
Figure 3. Investigation of the macroscopic morphology via light microscopy (LM) reveals the inhomogeneous drying behaviour via post-drying with pinholes (orange) and the homogeneous and dense thin film of the instant- and pre-dried area (green and red) a). Investigation of the microscopic morphology via scanning electron microscopy (SEM) reveals that grain sizes (diameters (d) presented on the upper left corner of SEM images) are significantly larger in the instant-drying region (green) than during post- and pre-drying (orange and red) b). Consistently, device performances of test PCEs of PSCs fabricated with these morphologies are highest in the case of instant-drying (see JV-curves in the bottom) c). External Quantum Efficiency (EQE) measurement for J_{sc} verification of all shown perovskite solar cells were either within 3 % of the value extracted from the JV-curves or corrected by the respective mismatch factor. For further details of the PCE-spread for solar cells built from respective drying regions, see Table 1.

Not only are these recordings demonstrating the accurate correlation of the position of the drying front with the evolving thin film morphology as predicted by the drying models, but further show its direct impact on the achievable PCE of perovskite test devices. Furthermore, the high-quality, homogenous morphology formation of instantly dried thin films has a direct impact on the resulting improved devices' PCE stability compared to solar cells built from pre- and post-drying thin films. Further information of the respective thin film morphology formation having an impact on stability during more than 100 days after fabrication is given in Figure S6, Supporting Information. Additionally, this demonstrates the importance of an adequate observation and suppression of the gas backflow inducing pre-drying. In conclusion, we confirmed the correlation of the quenching positions – which are indicated by recording a video of the "drying front" with a CCD camera – and the morphology formation of the fabricated thin films as well as the performance of fabricated solar cells. This interrelation validates that a certain threshold of mass transfer coefficient must be present at critical thin film thickness, which is correlated with the critical concentration/supersaturation.

Table 1. Device performances of champion cells as well as mean values and standard deviations of PCE, FF, J_{sc} and V_{oc} of PSCs fabricated with the according morphologies depicted in Figure 3 (orange, green and red framed).

	post-drying (orange)	instant-drying (green)	pre-drying (red)
Champion-PCE [%]	8.6	18.6	14.5
Ø PCE [%]	6.3 ± 1.3	18.1 ± 0.3	13.5 ± 0.7
Ø FF [%]	36.3 ± 2.2	69.7 ± 0.9	63.4 ± 2.0
Ø Jsc [mA cm^{-2}]	16.8 ± 0.7	20.9 ± 0.2	18.3 ± 0.5

Ø Voc [V]	0.89 ± 0.06	1.10 ± 0.01	0.99 ± 0.03

The champion PCE in the case of instant-drying reaches 18.6 %, whereas post- and pre-drying result in decreased performances. The mean values and standard deviations of the characteristic values calculated from each 10 representative cells of the according morphology, underline the importance of optimal prompt drying, showing higher mean values and lower variance for all values.

In order to enlarge the optimal instantly dried area (green), we limit the pre-drying, i.e., we improve gas backflow prevention by setup adjustments. According adjustments include an increased overlapping of the slot nozzle lips, exact control of the angle and optimal distance of the slot nozzle towards the substrate (optimized on the slot width) which all together result in a minimized gas backflow for the presented setup. However, the reduced slot nozzle height, which is a major parameter allowing the extension of the optimal instant-drying regime, blocks the view for the in situ characterization. Therefore time-resolved in situ data can not be provided.

Specifically, the gas backflow is partially suppressed by overlapping lips (0.5 cm), an exact height and angle control of the drying slot nozzle (0.3 cm and 15 °) at a slot width of 50 µm. However, a certain proportion of the gas backflow is inevitable, due to disturbing, but important functional and thereby difficult to eliminate components in the nozzle, the inside contour having edges and certain radii of curvature inducing stalling and turbulences of the gas flow as well as the tendency of air flowing from high to low pressure regions.[35,36] In summary, monitoring and evaluating the drying line being ahead of the center line leads to consequential adjustments of the slot nozzle so that the gas backflow can be partially suppressed. These slot nozzle adjustments, reducing the effect of pre-drying, maximize the optimal area of reproducible high-quality perovskite thin film and obtain upscaled high performances of PSCs achieving an overall homogeneous drying behavior on areas of 102 cm^2 (Figure 4, photographs).

2.3. Discriminating different drying front positions on separate substrates

As discussed in section 2.1 and 2.2, the timing of quenching for slot-die coated substrates is crucial for the optimal perovskite thin film formation. By varying the nitrogen flow ($u_0 = $ (a) $35\,\mathrm{m}\,\mathrm{s}^{-1}$, (b) $42\,\mathrm{m}\,\mathrm{s}^{-1}$ and (c) $50\,\mathrm{m}\,\mathrm{s}^{-1}$) and pinned drying speed ($2\,\mathrm{mm}\,\mathrm{s}^{-1}$), we test the hypothesis that the position of the drying front can be directly tuned with the gas flow speed (see Figure 4). Indeed, the morphology formation as well as the resulting performances of solar cells, built from incorporating parts of presented substrates, confirm that there is an optimal nitrogen flow rate for a given constant drying speed of slot-die coated upscaled areas with gas backflow prevention adjustments (see section 2.2). For the drying speed of $2\,\mathrm{mm}\,\mathrm{s}^{-1}$, a nitrogen flow rate of $42\,\mathrm{m}\,\mathrm{s}^{-1}$ is optimal (Figure 4) in terms of morphology formation reflected in the mean PCE of 17.5 % of PSCs fabricated on test areas of the respective substrate (b) bottom part.

In agreement with earlier observations (see section 2.1), we can distinguish the identified instant-, post- and pre-drying cases by their respective characteristic morphology formation and performance of solar cells fabricated on test areas (Figure 4 a),b),c).

In a nutshell: Post-drying (Figure 4 a) leads to the least homogeneous thin films and performances. However, too high N_2-flow induces – as discussed in section 2.1 and 2.2 – an inevitable gas backflow in scalable systems, which causes pre-drying of the thin film (Figure 4 c). Therefore, the drying front must also not deviate before the slot jet center (consistent with Figure 2 and 3). Ultimately – having the ideal wet thin film and minimized gas backflow – we validate an extended instant-drying regime and an optimum nitrogen flow rate while having a given drying speed with a performance maximum of > 18 % (Figure 4 b).
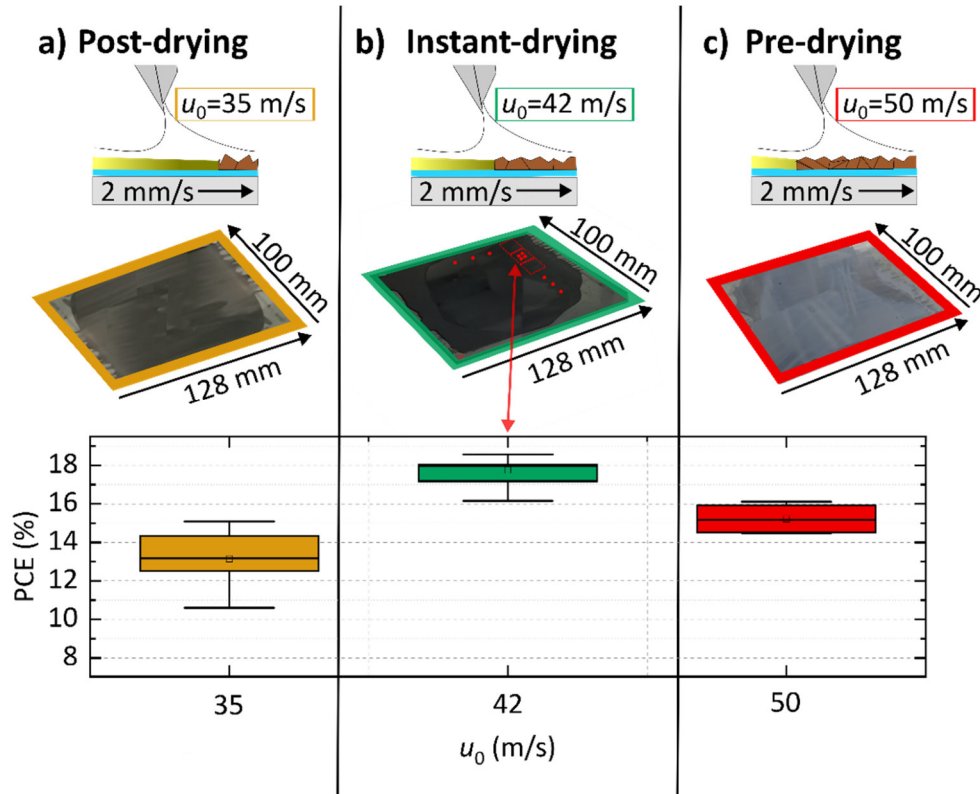
Figure 4. Photographs and PCEs of PSCs from devices fabricated on test areas of the respective substrate ($>100\,\text{cm}^2$). Perovskite absorber thin films are fabricated with the slot-die coating, gas quenching setup shown in Figure 1 at quenching gas flow velocities, u_0 (a) $35\,\text{m}\,\text{s}^{-1}$, (b) $42\,\text{m}\,\text{s}^{-1}$ and (c) $50\,\text{m}\,\text{s}^{-1}$ at constant coating speed $2\,\text{mm}\,\text{s}^{-1}$ and minimal quenching nozzle height of 3 mm. The reduced quenching nozzle height allows the extension of the optimal instant-drying regime but blocks the view for the in situ characterization. Consistently, with the observation on a single substrate (Figure 2 and 3), when u_0 is too low (a), the perovskite crystallizes significantly behind the gas nozzle (post drying), at optimal u_0 the perovskite crystallizes right at the center line (instant-drying) b), while at too high u_0 the perovskite crystallizes before reaching the maximum gas flow (pre-drying) c). Optimal morphology is only reached at $u_0 = 42\,\text{m}\,\text{s}^{-1}$, which reflects in the mean PCE of 17.5 % of PSCs with stack ITO/2Pacz/Per/C60/BCP/Ag fabricated on test areas of the respective substrate (bottom part).

2.4. Module fabrication on enlarged instant-drying regime

As introduced in section 2.3, the instant-drying regime can be extended and controlled via the gas flow. For a given drying speed, a clear optimum N_2 gas flow is apparent. Demonstrating the importance of adequate N_2 gas flow rates at a certain time for scalable techniques during one-step depositions, a 50x50 mm^2 is embedded in the instant-drying regime of the 98x128 mm^2 substrate and the perovskite deposited as demonstrated in section 2.3. The mini-modules have the classic P1, P2, and P3 scribes by a nanosecond laser scribing, generating a geometrical fill factor (GFF) of 95 % and consist of 9 sub solar cells with an active area of 144 mm^2 each (see Figure S3 Supporting Information). The identical stack with all-scalable methods as in section 2.2, only with thermally evaporated 75 nm gold back electrodes, is fabricated (see Experimental Section and Figure S5 Supporting Information). Remarkably, reproducible perovskite mini-modules with the perovskite absorber composition $Cs_{0.1}(FA_{0.83}MA_{0.17})_{0.9}(I_{0.83}Br_{0.17})_3$ can be fabricated. Due to the reduced slot nozzle height, which is a major parameter allowing the extension of the optimal instant-drying regime, the view for the in situ characterization is blocked. Therefore, time-resolved in situ data can not be provided. However, with this slot nozzle-adjusting strategy as a result of the in situ monitored backflow-preventing method, a PCE of 17.2 % on an active area of 1296 mm^2 is obtained (Figure 5 b).
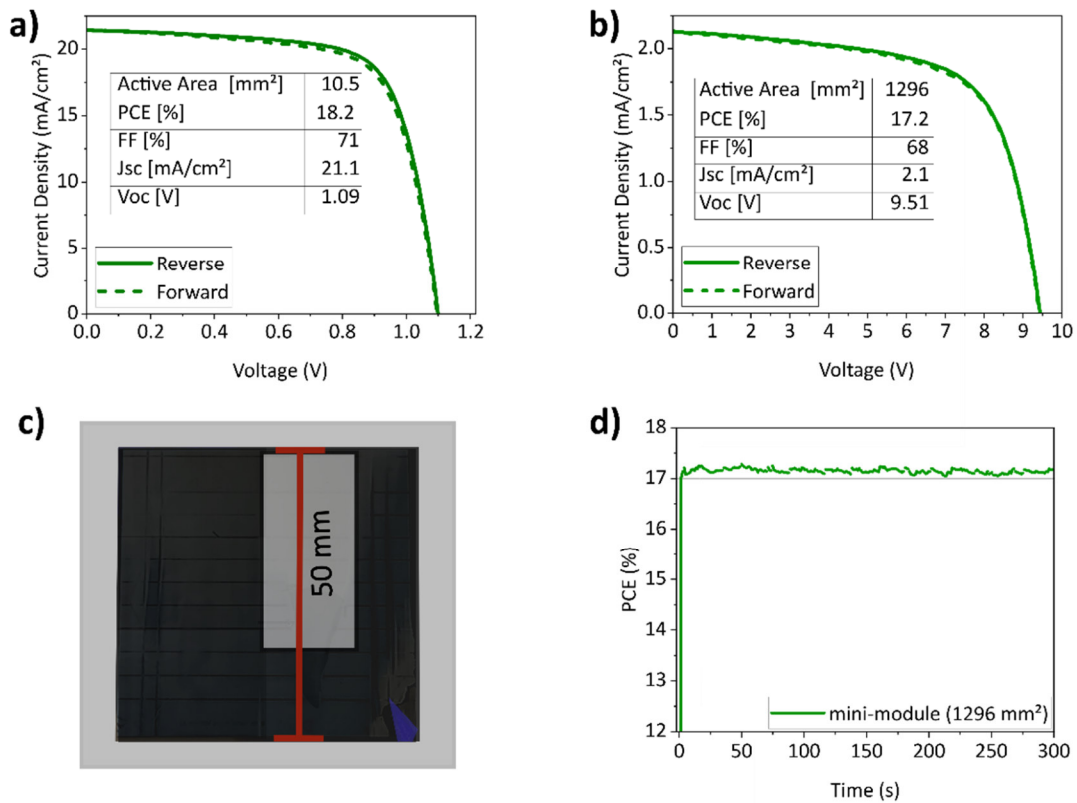
Figure 5. Device performance of a test PCE of PSCs (ITO/2Pacz/Per/C60/BCP/Au), fabricated

with the morphology in the case of instant-drying shows a PCE of 18.2 % on an active area of

10.5 mm² a). Device performance of a 50x50 mm² mini-module positioned in the optimal instant-

drying regime of the 128x98 mm² substrate on the same day, with identical coating and drying

conditions as well as the same precursor solution, shows only 5 % relative upscaling loss (17.2 %

on 1296 mm²) b). Consistently, a photograph of the mini-module on the perovskite side shows

the perovskite thin film after homogeneous drying with prompt crystallization c). Investigation

of the device performance reveals successfully PCE > 17.1 % during 5 minutes in the MPP d).

Compared to a simultaneously fabricated champion cell from a test area of the instant-drying

regime (active area of 10.5 mm²), showing a PCE of 18.2 %, only 5 % relative upscaling loss is

demonstrated, mainly explainable by module scribing and interconnection resistances. The characteristic values (Jsc, Voc, FF) of the mini-module, including 9 sub solar cells, show minimal deviation compared to the reference cell, implying a high homogeneity during the coating and drying process (see Figure 5 a) and b). More specifically, each sub solar cell of the mini-module has a Voc of ~1.06 V, which is close to the Voc obtained from the champion small-scale PSC (1.09 V). This small deviation indicates excellent homogeneity over the entire module area of the perovskite thin film and good interfaces of the stack with all-scalable methods (see Figure S5 Supporting Information). The detailed information of the perovskite solar module is shown in Figure 5 b) and the efficiency deviation among the sub solar cells themselves in Table S1 (Supporting Information), confirming homogeneity over the entire module area. The champion device's efficiency distribution of 9 sub solar cells shows that all sub solar cells of the module have a PCE above 17 %, validating excellent drying conditions and homogeneity over the entire module area. Reproducibility is demonstrated by fabricating 5 modules separately with the same precursor solution and identical drying conditions. The mean value of the PCE (øPCE) reaches 17.1 ± 0.1 % (detailed information in Table S1 Supporting Information). Conclusively, demonstrating controlled morphology formation as depicted in Figure 5 c), enables fabrication of high-performing perovskite mini-module with only small upscaling loss and with a stable output of PCE > 17.1 % during the 5 minutes MPP tracking measurement (Figure 5 d) with scalable deposition and drying techniques.

2.5. Prospect for industrial fabrication based on the insight into drying behavior

The upscaling process represents one of the major challenges to push perovskite PV to an industrial level. The method presented above is a step forward to a systematic, universal and adequate industrial process in a sense that it could be applied to drying processes of perovskite solution thin films of any size. However, in terms of industrial applicability of perovskite solution processed perovskite PV, this method with the specific setup of one slot-die head in combination with one slot nozzle still exhibits some challenging features.

- First, the optimal web speed for coating and drying vary, which complicates a continuous processing, i.e., requires to separate the coating and drying line. In this work, process windows of coating and drying still differentiate by a factor of 3, which would lead to problems in linear fabrication processes.

- Second, the web speeds which are included in this work are only in the order of magnitude of $\sim$mm s^{-1}. For an industrial fabrication, values in order of cm s^{-1} – m s^{-1} are required.[37]

- Third, the maximal heat transfer coefficient of $\sim$50 W m^{-2} K^{-1} in typical industrial-scale convection dryers is about one order of magnitude below those required during drying perovskite precursors.[34] We take the heat transfer coefficient as a reference for the gas quenching (not including annealing) process, since the preceded model of drying dynamics is based on local heat transfer measurements.[12,32]

In order to address the challenges of continuous processing and industrial fabrication relating to requirements of the web speed, we note, first of all, that the method itself does not at all limit the coating and drying speed. However, solvent systems in combination with the restriction of laboratory setup sites have a limiting effect, e.g., in terms of throughputs. The limited space issue

in a regular sized glovebox (internal volume $\sim 4\,m^3$) and high operating costs maintaining the inert atmosphere can be overcome by a well-designed fume hood or replacing the toxic solutes by non-hazardous ones. To date, the use of toxic solutes is still an issue which hinders paving the way for industrial-scale commercialization of thin film perovskite photovoltaics, due to e.g., an increased requirement of safety precautions for manufacturers and the environment. However, it is highlighted that the use of toxic solvents can be avoided. The implementation of green and sustainable perovskite precursor solvent systems, such as nonhazardous solvents (mostly DMSO-based)/alcohol/acid systems is an ongoing research topic and are in constant evaluation of their comparability to the toxic counterparts.[38–42] Different alternative industry-friendly solvent systems for processing the perovskite absorber are nowadays investigated and compared to their toxic counterparts, e.g., in respect to the upscaling processability in an ambient environment or multifunctionality due to semipolar characteristics.[43,44]

Subsequent to steps towards spatial expansion, a simple way to increase the web speed is to increase the distance between the slot-die coater and the slot nozzle and invest in nonlinear processes. Another possibility is inserting a second slot nozzle prior to the first with a wider slot to pre-dry the solution thin film homogenously and then inducing the nucleation with a narrow slot nozzle. The web speeds can be aligned with this additional parameter. Finally, additives can affect the fluidic behavior and the nucleation process, specifically aligning the drying to the coating speed in optimal case. Consequently, in all three cases, the right timing of a certain threshold heat (and accordingly mass) transfer directly underneath the narrow slot nozzle being present at the critical thin film thickness, will require a very precise tuning of the drying parameters. In this context, the proven concept of the correlation of the drying front and yielded performance is a particularly interesting indicator to possibly automate and control the process immediately without wasting

time and effort during the arduous production line. In the future, such a routine can rapidly identify a drift in the resulting morphology such that, for example, the gas flow velocity can be fine-tuned and thereby, re-optimized immediately in an automated feedback loop.

Regarding the third challenge of the maximal heat transfer coefficient in industrial dryers, utilizing narrow slot nozzles is a simple and effective approach. However, this implies that the mass transfer coefficient will have a very narrow peak to which the drying parameters need to be fine-tuned. So far, this is mainly the drying speed and the gas flow velocity, since other solutions, e.g., increasing the temperature will increase the crystal growth rate, which has an adverse effect for obtaining nucleation-dominated morphologies. One alleviating strategy can be the usage of lower boiling point solvents. Since these evaporate faster, nucleation gets more dominant towards crystal growth compared to high boiling solvents, even at lower mass transfer coefficients. However, such solvent systems are potentially more toxic which interferes with the prior encountering methods and the general way to industrial processing. Additionally, they are rarely applied in developing new spin-coating recipes and can have solution stability issues.[45]

3. Conclusion

This work addresses the transfer of solution-processed perovskite thin film deposition to large-area coating and gas-assisted drying processes. It implements, demonstrates and validates the predictability of the morphology formation for dedicated gas dryer systems including those developed in the future for industrial-scale perovskite photovoltaics production lines. We demonstrate the fundamental interrelation between drying dynamics and the quality of slot-die coated gas quenched perovskite thin films with precisely defined drying conditions and in situ monitoring. Thereby, we identify and validate the critical parameters needed in the dryer design

for upscaling, which are, (i) after tracking the quenching positions for a given material composition and setup geometry, an adequate strong gas flow (in this case 42 m s^{-1}) inducing prompt crystallization, (ii) the adjusted design of a slot nozzle according the aero- and drying dynamics for gas backflow prevention, including overlapping lips, a dynamic height and angle control for a given slot width and (iii) fine-tuning of the gas flow velocity to the applied drying speed for the enlarged optimal instant-drying regime, possible by direct in situ monitoring.

Within this work, we address the question how oblique impinging slot jet drying with high pressure gas, controlled height, angle and an overlapping lip configuration can be implemented in an upscaling setup and evaluated in the sense of predicting coating windows for dynamic perovskite solution printing in terms of the drying speed and gas flow velocity. For this purpose, we monitor the ideally prompt crystallization process with a CCD camera and categorize the morphological differences of different drying behaviors on a single substrate distinguishing pre-, post- and instant-drying. By tracking the exact line of quenching positions, defined as "drying front", fundamental interrelations of setup parameters with the morphology formation of fabricated thin films as well as the resulting performance of corresponding solar cells are validated. We increase the PCE to >18% on an overall area of >100cm^2.

The results are consistent with an analytical model of the drying dynamics of perovskite solution thin films on small area.[12,32] This model states, that a certain mass transfer coefficient must be present at a critical thin film thickness (correlated to the critical concentration/supersaturation). Correlating the experimental fabrication of perovskite thin films on an area of >100 cm^2 with the model, we succeed in validating the upscaling criterion, that the drying front needs to be directly at the center line. More precisely, we validate that the morphology evolution is optimal exactly

when there is a specifically high mass transfer needed at the position where the wet thin film passes the critical solute concentration to induce rapid drying and a high nucleation rate (see section 2.1).

We show that the optimally quenched area can be controlled by adjusting drying parameters according to the drying front. Thereby, we derive practical design guidelines for the drying setup such as the adjusted design of the slot nozzle according the aero- and drying dynamics, mainly for gas backflow prevention (see section 2.2).

At the adjusted setup, the position of the drying front can be directly tuned with the gas flow velocity at a given drying speed, resulting in an optimal instant-drying regime on large-area (see section 2.3). We demonstrate homogeneity and reproducibility by fabricating $50x50\,mm^2$ mini-modules, which are laser scribed within the instant-drying regime, with a reproducible average PCE over 17%. The mini-modules show only minimal area loss to the reference cells (18.2%), due to module scribing and interconnection resistances. (see section 2.4)

The practical guidelines – backed by in situ process surveillance – enhance the facilitation for industrial production, such that fine-tuned dryers can be integrated within the production line. Therefore, there is no necessity to manually interrupt production for an extra step of drying. The results of this work imply the validation of successful prediction of parameter spaces (e.g., web speed and gas flow velocity) for scalable, dynamic operation of perovskite fabrication lines. The parameter optimization is tested in an extensive correlative study with experimentally fabricated and characterized perovskite thin films, underlining the validity of the proposed methodology.

4. Experimental Section

Preparation of triple cation perovskite solution:

The precursor solution is prepared by mixing PbI_2 (1.1 M, Alfa Aesar, Ultra dry), $CH(NH_2)_2I$ (FAI, 1 M, GreatCell Solar), $PbBr_2$ (0.2 M, TCI Chemicals) and CH_3NH_3Br (MABr, 0.2 M, GreatCell Solar) with N,N-Dimethylformamide (DMF, Sigma-Aldrich) and Dimethylsulfoxide (DMSO, Sigma-Aldrich) in the v:v ratio 4:1. Subsequently, 89 μL per mL solution of CsI (1.5 M, Alfa Aesar) dissolved in DMSO are added and vigorously agitated until all the powders are dissolved. The solidified perovskite composition is $Cs_{0.1}(FA_{0.83}MA_{0.17})_{0.9}(I_{0.83}Br_{0.17})_3$ with a bandgap of ~1,65 eV. On the day of deposition, 4 mg per mL of urea (CH_4N_2O, SigmaAldrich) is added [46], altogether representing the basic perovskite solution. The basic perovskite solution is diluted in the ratio 2.5:1 in 4:1 DMF (Sigma-Aldrich):DMSO (Sigma-Aldrich) for SDC and is used in its concentrated form for spin coating references in order, to guarantee similar thin film thicknesses. The basic solution is no older than one week.

Processing of samples for coating experiments:

128x128 mm² ITO substrates (Luminescence Technology, sheet resistance $15\,\Omega\,sq^{-1}$) are cleaned in an ultrasonic bath for 10 min in acetone and isopropanol, respectively. Subsequently, they are plasma etched for 3 min. Then, the samples are placed in the setup depicted in Figure 1. The coating is performed with a slot-die coater (length 100 mm) and constant parameters (velocity 6 $mm\,s^{-1}$ and gap width 150 μm). Subsequently, the movable table is driven underneath the slot jet and the web speed is changed to the respective value and the N_2-flow is initiated with the chosen gas velocity u_0. After the coating and quenching, the substrates are annealed for 55 min at 100 °C.

Processing of perovskite solar cells:

128x128 mm² ITO substrates (Luminescence Technology, sheet resistance $15\,\Omega\,sq^{-1}$) are laser structured (see SI), cut into 128x98 mm² substrates and then precut into a 6x6 grid of 16x16 mm² substrates. Afterwards, they are cleaned in an ultrasonic bath for 10 min in acetone and isopropanol, respectively and plasma etched for 3 min. Subsequently, the hole transport layer $C_{14}H_{14}NO_3P$ (2PACz, 6 nm thick, TCI Chemicals) is thermally evaporated and deposited using a thermal evaporation system at a pressure of 5×10^{-7} mbar with a deposition rate of 0.05-$0.2\,A\,s^{-1}$. Then, the perovskite coating experiment is conducted as explained above. Afterwards, the substrates are cut into 36 respective 16x16 mm² substrates and sorted by nucleation and growth-dominated regions if required. The device fabrication is completed by thermally evaporating and depositing the electron transport layer – Fullerene (C60, 25 nm thick, Alfa Aesar) and bathocuproine (BCP, 5 nm thick, Luminescence Technology) – using a thermal evaporation system at a pressure of 5×10^{-7} mbar with a deposition rate of 0.4 and $0.3\,A\,s^{-1}$, respectively. Finally, the back electrode ($100\,nm$ Ag with $1\,A\,s^{-1}$) was thermally evaporated with a shadow mask in a thermal evaporator. The active area of the solar cells is $10.5\,mm^2$, if not stated otherwise.

Current Density−Voltage (J−V) Measurements:

The J−V measurements are performed under AM 1.5G conditions. The stabilized PCE of the cells is determined by the power output at a voltage close to the MPP under continues illumination for 5 min. A shadow mask is used in order to define the active area. External Quantum Efficiency (EQE) measurement for Jsc verification of all shown perovskite solar cells were either within 3 % of the value extracted from the JV-curves or corrected by the respective mismatch factor. Detailed information can be found in [47].

ASSOCIATED CONTENT

Supporting Information.

The following files are available free of charge from the author (in one PDF).

Figures – Additional detailed schematic of the in-house setup (S1), photographs of the experimental setup (S2), graphical illustration of the laser scribed module area and interconnections (S3), schematic of the embedded module within the slot-die coated substrate (S4), schematic illustration of the layer stack fabricated with all-scalable methods (S5), MPP-measurement data of solar cells built from different drying regimes on progressing days (S6), XRD-measurements of perovskite thin films from different drying regimes (S7)

Equation – formula for the relative upscaling loss per decade (S1)

Table – Champion module performance distribution of 9 sub solar cells as well as mean values and standard deviations of the PCE calculated from 5 modules (S1)

Video – Link to explanatory drying video (S1)

AUTHOR INFORMATION

Corresponding Author

*Ulrich W. Paetzold

E-mail: ulrich.paetzold@kit.edu

Author Contributions

The manuscript was written through contributions of all authors. All authors have given approval to the final version of the manuscript.

Funding Sources

ACKNOWLEDGMENT

ABBREVIATIONS

PCE, power conversion efficiency; PSCs, perovskite solar cells; PV, photovoltaic, CdTe, cadmium telluride; CIGS, copper indium gallium selenide; GaAs, gallium arsenide; R2R, roll-to-

roll; SD, slot-die; N_2, nitrogen; CCD, charge-coupled device; LM, light microscopy; SEM, scanning electron microscope/microscopy; FF, fill factor; Jsc, short-circuit current density; Voc, open-circuit voltage; øPCE, mean value of the PCE; EQE, External Quantum Efficiency; SDC, slot-die coating.

REFERENCES

(1) NREL. *Best Research-Cell Efficiencies*. https://www.nrel.gov/pv/assets/pdfs/cell-pv-eff-emergingpv.pdf (accessed 2023-02-10).

(2) Verma, A. K. Challenges and Potential of Perovskite Solar Cells. *Journal of Ravishankar University (JRUB)* **2022**, *35* (2), 68–75. DOI: 10.52228/JRUB.2023-35-2-6.

(3) Zhao, Y.; Zhao, C.; Chen, X.; Luo, T.; Ding, M.; Ye, T.; Zhang, W.; Chang, H. Air-Processed and Mixed-Cation Single Crystal Engineering-Based Perovskite Films for Efficient and Air-Stable Perovskite Solar Cells. *J. Mater. Sci.: Mater. Electron.* **2020**, *31* (3), 2167–2176. DOI: 10.1007/s10854-019-02742-7.

(4) Garside, M. *Silicon - Statistics & Facts Statista*. https://www.statista.com/topics/1959/silicon (accessed 2022-11-25).

(5) Mann, S. A.; Wild-Scholten, M. J. de; Fthenakis, V. M.; van Sark, W. G.; Sinke, W. C. The Energy Payback Time of Advanced Crystalline Silicon PV Modules in 2020: A Prospective Study. *Prog. Photovolt.: Res. Appl.* **2014**, *22* (11), 1180–1194. DOI: 10.1002/pip.2363.

(6) Moffeq Alobaidi, M.; Thabit, N. M. M. The Impact of Employed Solar Systems in Architectural Projects Facades. *Zanco Journal of Pure and Applied Sciences (ZJPAS)* **2019**, *31* (s3), 84–88. DOI: 10.21271/zjpas.31.s3.12.

(7) Deb, D.; Bhargava, K. Degradation, Mitigation, and Forecasting Approaches in Thin Film Photovoltaics. *Elsevier Academic Press*, **2022**. DOI: 10.1016/C2020-0-00458-5.

(8) Ajibade, P. A.; Adeloye, A. O.; Oluwalana, A. E.; Thamae, M. A. Organolead Halide Perovskites: Synthetic Routes, Structural Features, and Their Potential in the Development of Photovoltaic. *Nanotechnology Reviews* **2023**, *12* (1). DOI: 10.1515/ntrev-2022-0547.

(9) Nayak, P. K.; Mahesh, S.; Snaith, H. J.; Cahen, D. Photovoltaic Solar Cell Technologies: Analysing the State of the Art. *Nat. Rev. Mater.* **2019**, *4* (4), 269–285. DOI: 10.1038/s41578-019-0097-0.

(10) NREL. *Best Research-Cell Efficiencies Chart*. https://www.nrel.gov/pv/cell-efficiency.html (accessed 2023-09-20).

(11) Xu, K.; Al-Ashouri, A.; Peng, Z.-W.; Köhnen, E.; Hempel, H.; Akhundova, F.; Marquez, J. A.; Tockhorn, P.; Shargaieva, O.; Ruske, F.; Zhang, J.; Dagar, J.; Stannowski, B.; Unold, T.; Abou-Ras, D.; Unger, E.; Korte, L.; Albrecht, S. Slot-Die Coated Triple-Halide Perovskites for Efficient and Scalable Perovskite/Silicon Tandem Solar Cells. *ACS Energy Letters* **2022**, *7* (10), 3600–3611. DOI: 10.1021/acsenergylett.2c01506.

(12) Ternes, S.; Börnhorst, T.; Schwenzer, J. A.; Hossain, I. M.; Abzieher, T.; Mehlmann, W.; Lemmer, U.; Scharfer, P.; Schabel, W.; Richards, B. S.; Paetzold, U. W. Drying Dynamics of Solution-Processed Perovskite Thin-Film Photovoltaics: In Situ Characterization, Modeling, and Process Control. *Advanced Energy Materials* **2019**, *9* (39). DOI: 10.1002/aenm.201901581.

(13) Yang, F.; Jang, D.; Dong, L.; Qiu, S.; Distler, A.; Li, N.; Brabec, C. J.; Egelhaaf, H.-J. Upscaling Solution-Processed Perovskite Photovoltaics. *Advanced Energy Materials* **2021**, *11* (42), 2101973. DOI: 10.1002/aenm.202101973.

(14) Ritzer, D. B.; Abzieher, T.; Basibüyük, A.; Feeney, T.; Laufer, F.; Ternes, S.; Richards, B. S.; Bergfeld, S.; Paetzold, U. W. Upscaling of Perovskite Solar Modules: The Synergy of Fully Evaporated Layer Fabrication and All-Laser-Scribed Interconnections. *Progress in Photovoltaics: Research and Applications* **2022**, *30* (4), 360–373. DOI: 10.1002/pip.3489.

(15) Verma, A.; Martineau, D.; Hack, E.; Makha, M.; Turner, E.; Nüesch, F.; Heier, J. Towards Industrialization of Perovskite Solar Cells Using Slot Die Coating. *Journal of Materials Chemistry C* **2020**, *8* (18), 6124–6135. DOI: 10.1039/D0TC00327A.

(16) Benkreira, H.; Ikin, J. B. Slot Coating Minimum Film Thickness in Air and in Rarefied Helium. *Chemical Engineering Science* **2016**, *150*, 66–73. DOI: 10.1016/j.ces.2016.04.053.

(17) Peng, Z.-W.; Xu, K.; Bournazou, A. C.; Unger, E.; Albrecht, S.; Stannowski, B. Upscaling of Perovskite/C-Si Tandem Solar Cells by Using Industrial Adaptable Processes. *SiliconPV 2022, The 12TH International Conference on Crystalline Silicon Photovoltaics*; AIP Publishing **2023**, p 90003. DOI: 10.1063/5.0141139.

(18) Rana, P. J. S.; Febriansyah, B.; Koh, T. M.; Muhammad, B. T.; Salim, T.; Hooper, T. J. N.; Kanwat, A.; Ghosh, B.; Kajal, P.; Lew, J. H.; Aw, Y. C.; Yantara, N.; Bruno, A.; Pullarkat, S. A.; Ager, J. W.; Leong, W. L.; Mhaisalkar, S. G.; Mathews, N. Alkali Additives Enable Efficient Large Area (>55 cm 2) Slot-Die Coated Perovskite Solar Modules. *Adv. Funct. Materials* **2022**, *32* (22), 2113026. DOI: 10.1002/adfm.202113026.

(19) NREL. *Champion Module Efficiencies*. https://www.nrel.gov/pv/module-efficiency.html (accessed 2023-03-10).

(20) Valsalakumar, S.; Roy, A.; Mallick, T. K.; Hinshelwood, J.; Sundaram, S. An Overview of Current Printing Technologies for Large-Scale Perovskite Solar Cell Development. *Energies* **2023**, *16* (1), 190. DOI: 10.3390/en16010190.

(21) Ding, X.; Liu, J.; Harris, T. A. L. A Review of the Operating Limits in Slot Die Coating Processes. *AIChE Journal* **2016**, *62* (7), 2508–2524. DOI: 10.1002/aic.15268.

(22) Schötz, K.; Greve, C.; Langen, A.; Gorter, H.; Dogan, I.; Galagan, Y.; van Breemen, A. J. J. M.; Gelinck, G. H.; Herzig, E. M.; Panzer, F. Understanding Differences in the Crystallization Kinetics between One-Step Slot-Die Coating and Spin Coating of MAPbI 3 Using Multimodal In Situ Optical Spectroscopy. *Advanced Optical Materials* **2021**, *9* (21), 2101161. DOI: 10.1002/adom.202101161.

(23) Liang, X.; Zhou, X.; Ge, C.; Lin, H.; Satapathi, S.; Zhu, Q.; Hu, H. Advance and Prospect of Metal-Organic Frameworks for Perovskite Photovoltaic Devices. *Organic Electronics* **2022**, *106*, 106546. DOI: 10.1016/j.orgel.2022.106546.

(24) Yu, Y.; Zhang, F.; Hou, T.; Sun, X.; Yu, H.; Zhang, M. A Review on Gas-Quenching Technique for Efficient Perovskite Solar Cells. *Solar RRL* **2021**, *5* (10), 2100386. DOI: 10.1002/solr.202100386.

(25) Taherimakhsousi, N.; Fievez, M.; MacLeod, B. P.; Booker, E. P.; Fayard, E.; Matheron, M.; Manceau, M.; Cros, S.; Berson, S.; Berlinguette, C. P. A Machine Vision Tool for

Facilitating the Optimization of Large-Area Perovskite Photovoltaics. *npj Comput. Mater.* **2021**, *7* (1), 1–10. DOI: 10.1038/s41524-021-00657-8.

(26) Tang, S.; Bing, J.; Zheng, J.; Tang, J.; Li, Y.; Mayyas, M.; Cho, Y.; Jones, T. W.; Yang, T. C.-J.; Yuan, L.; Tebyetekerwa, M.; Nguyen, H. T.; Nielsen, M. P.; Ekins-Daukes, N. J.; Kalantar-Zadeh, K.; Wilson, G. J.; McKenzie, D. R.; Huang, S.; Ho-Baillie, A. W. Complementary Bulk and Surface Passivations for Highly Efficient Perovskite Solar Cells by Gas Quenching. *Cell Reports Physical Science* **2021**, *2* (8), 100511. DOI: 10.1016/j.xcrp.2021.100511.

(27) Babayigit, A.; D'Haen, J.; Boyen, H.-G.; Conings, B. Gas Quenching for Perovskite Thin Film Deposition. *Joule* **2018**, *2* (7), 1205–1209. DOI: 10.1016/j.joule.2018.06.009.

(28) Cotella, G.; Baker, J.; Worsley, D.; Rossi, F. de; Pleydell-Pearce, C.; Carnie, M.; Watson, T. One-Step Deposition by Slot-Die Coating of Mixed Lead Halide Perovskite for Photovoltaic Applications. *Solar Energy Materials and Solar Cells* **2017**, *159*, 362–369. DOI: 10.1016/j.solmat.2016.09.013.

(29) Fievez, M.; Singh Rana, P. J.; Koh, T. M.; Manceau, M.; Lew, J. H.; Jamaludin, N. F.; Ghosh, B.; Bruno, A.; Cros, S.; Berson, S.; Mhaisalkar, S. G.; Leong, W. L. Slot-Die Coated Methylammonium-Free Perovskite Solar Cells with 18% Efficiency. *Solar Energy Materials and Solar Cells* **2021**, *230*, 111189. DOI: 10.1016/j.solmat.2021.111189.

(30) Howard, I. A.; Abzieher, T.; Hossain, I. M.; Eggers, H.; Schackmar, F.; Ternes, S.; Richards, B. S.; Lemmer, U.; Paetzold, U. W. Coated and Printed Perovskites for Photovoltaic Applications. *Advanced Materials* **2019**, *31* (26), e1806702. DOI: 10.1002/adma.201806702.

(31) Park, J.; Cho, J. Advances in Understanding Mechanisms of Perovskites and Pyrochlores as Electrocatalysts using In-Situ X-ray Absorption Spectroscopy. *Angewandte Chemie International Edition* **2020**, *59* (36), 15314–15324. DOI: 10.1002/anie.202000768.

(32) Ternes, S.; Mohacsi, J.; Lüdtke, N.; Pham, H. M.; Arslan, M.; Scharfer, P.; Schabel, W.; Richards, B. S.; Paetzold, U. W. Drying and Coating of Perovskite Thin Films: How to Control the Thin Film Morphology in Scalable Dynamic Coating Systems. *ACS Applied Materials & Interfaces* **2022**, *14* (9), 11300–11312. DOI: 10.1021/acsami.1c22363.

(33) Li, J.; Dagar, J.; Shargaieva, O.; Maus, O.; Remec, M.; Emery, Q.; Khenkin, M.; Ulbrich, C.; Akhundova, F.; Márquez, J. A.; Unold, T.; Fenske, M.; Schultz, C.; Stegemann, B.; Al-Ashouri, A.; Albrecht, S.; Esteves, A. T.; Korte, L.; Köbler, H.; Abate, A.; Többens, D. M.; Zizak, I.; List-Kratochvil, E. J. W.; Schlatmann, R.; Unger, E. Ink Design Enabling Slot-Die Coated Perovskite Solar Cells with >22% Power Conversion Efficiency, Micro-Modules, and 1 Year of Outdoor Performance Evaluation. *Advanced Energy Materials* **2023**, *13* (33). DOI: 10.1002/aenm.202203898.

(34) Cavadini, P.; Scharfer, P.; Schabel, W. Investigation of Heat Transfer within an Array of Impinging Jets with Local Extraction of Spent Fluid. *Proceedings of the 15th International Heat Transfer Conference, IHTC* **2014**. DOI: 10.1615/IHTC15.mtr.008875.

(35) Satheesha, V.; Muralidhra, B. K.; Abhilash, N; Umesh, C. K. Flow Visualization of Rectangular Slot Air Jet Impingement on Flat Surfaces. *International Journal of Engineering Sciences & Research Technology* **2018**, *7* (1), 325–337. DOI: 10.5281/zenodo.1147471.

(36) Wang, J.; Klinkberg, T.; Teschner, M.; Weirich, D.; Koll, T. Simulation and Optimisation of a Wiping Knife on the Lab Scale. *12th International Conference on Zinc & Zinc Alloy Coated Steel Sheet*, **2021**, ASMET, ISBN 978-3-200-07779-9.

(37) Rolston, N.; Sleugh, A.; Chen, J. P.; Zhao, O.; Colburn, T. W.; Flick, A. C.; Dauskardt, R. H. Perspectives of Open-Air Processing to Enable Perovskite Solar Cell Manufacturing. *Front. Energy Res.* **2021**, *9*, 684082. DOI: 10.3389/fenrg.2021.684082.

(38) Miao, Y.; Ren, M.; Chen, Y.; Wang, H.; Chen, H.; Liu, X.; Wang, T.; Zhao, Y. Green Solvent Enabled Scalable Processing of Perovskite Solar Cells with High Efficiency. *Nature Sustainability* **2023.** DOI: 10.1038/s41893-023-01196-4.

(39) Cheng, J.; Fan, Z.; Dong, J. Research Progress of Green Solvent in CsPbBr3 Perovskite Solar Cells. *Nanomaterials (Basel, Switzerland)* **2023**, *13* (6). DOI: 10.3390/nano13060991.

(40) Wang, Y.; Shi, Z.; Wang, Y.; Khan, Q. U.; Li, X.; Deng, L.; Pan, Y.; Zhang, X.; Yang, Y.; Yue, X.; Hu, T.; Liu, F.; Wang, H.; Li, C.; Liu, K.; Yuan, W.; Cong, C.; Yu, A.; Zhan, Y. Intermediate Phase Free α-FAPbI3 Perovskite via Green Solvent Assisted Perovskite Single Crystal Redissolution Strategy. *Advanced Materials* **2023**, e2302298. DOI: 10.1002/adma.202302298.

(41) Wang, J.; Di Giacomo, F.; Brüls, J.; Gorter, H.; Katsouras, I.; Groen, P.; Janssen, R. A. J.; Andriessen, R.; Galagan, Y. Highly Efficient Perovskite Solar Cells Using Non-Toxic Industry Compatible Solvent System. *Solar RRL* **2017**, *1* (11). DOI: 10.1002/solr.201700091.

(42) Gardner, K. L.; Tait, J. G.; Merckx, T.; Qiu, W.; Paetzold, U. W.; Kootstra, L.; Jaysankar, M.; Gehlhaar, R.; Cheyns, D.; Heremans, P.; Poortmans, J. Nonhazardous Solvent Systems for Processing Perovskite Photovoltaics. *Advanced Energy Materials* **2016**, *6* (14), 1600386. DOI: 10.1002/aenm.201600386.

(43) Cho, J.; Kim, B.; Ryu, S.; Yun, A. J.; Gil, B.; Lim, J.; Kim, J.; Kim, J.; Park, B. Multifunctional Green Solvent for Efficient Perovskite Solar Cells. *Electron. Mater. Lett.* **2023**, *19* (5), 462–470. DOI: 10.1007/s13391-023-00410-x.

(44) Huang, S.-H.; Tian, K.-Y.; Huang, H.-C.; Li, C.-F.; Chu, W.-C.; Lee, K.-M.; Huang, Y.-C.; Su, W.-F. Controlling the Morphology and Interface of the Perovskite Layer for Scalable High-Efficiency Solar Cells Fabricated Using Green Solvents and Blade Coating in an Ambient Environment. *ACS Applied Materials & Interfaces* **2020**, *12* (23), 26041–26049. DOI: 10.1021/acsami.0c06211.

(45) Li, J.; Dagar, J.; Shargaieva, O.; Flatken, M. A.; Köbler, H.; Fenske, M.; Schultz, C.; Stegemann, B.; Just, J.; Többens, D. M.; Abate, A.; Munir, R.; Unger, E. 20.8% Slot-Die Coated MAPbI 3 Perovskite Solar Cells by Optimal DMSO-Content and Age of 2-ME Based Precursor Inks. *Advanced Energy Materials* **2021**, *11* (10). DOI: 10.1002/aenm.202003460.

(46) Farag, A.; Schmager, R.; Fassl, P.; Noack, P.; Wattenberg, B.; Dippell, T.; Paetzold, U. W. Efficient Light Harvesting in Thick Perovskite Solar Cells Processed on Industry-Applicable Random Pyramidal Textures. *ACS Applied Energy Materials* **2022**, *5* (6), 6700–6708. DOI: 10.1021/acsaem.1c04028.

(47) Gharibzadeh, S.; Hossain, I. M.; Fassl, P.; Nejand, B. A.; Abzieher, T.; Schultes, M.; Ahlswede, E.; Jackson, P.; Powalla, M.; Schäfer, S.; Rienäcker, M.; Wietler, T.; Peibst, R.; Lemmer, U.; Richards, B. S.; Paetzold, U. W. 2D/3D Heterostructure for Semitransparent Perovskite Solar Cells with Engineered Bandgap Enables Efficiencies Exceeding 25% in Four-Terminal Tandems with Silicon and CIGS. *Advanced Functional Materials* **2020**, *30* (19). DOI: 10.1002/adfm.201909919.

Table of Contents

TOC